Combined Two-Photon Calcium Imaging and Single-Ommatidium Visual Stimulation to Study Fine-Scale Retinotopy in Insects

Ying Zhu and Fabrizio Gabbiani

Abstract

Individual neurons in several sensory systems receive synaptic inputs organized according to subcellular topographic maps, yet the fine structure of this topographic organization has not been studied in detail. The lobula giant movement detector (LGMD) neuron in the locust visual system is known to receive topographic (retinotopic) excitatory inputs on part of its dendritic tree. To study the fine structure of this retinotopic mapping of visual inputs onto the excitatory dendritic field of the LGMD, we designed a custom microscope allowing visual stimulation at the native sampling resolution of the locust compound eye (defined by a single ommatidium or facet) while simultaneously performing two-photon calcium imaging on excitatory dendrites. Our goal is to provide the reader detailed guidelines on how to build a custom two-photon microscope and a single-facet stimulation setup, and to show experimental results on the detailed retinotopic structure of the projection of excitatory inputs onto the LGMD based on these tools.

1. Introduction

1.1 Two-Photon Microscopy

Starting in the 19th century, staining techniques combined with optical imaging of brain tissue initiated the investigation of the morphology of individual neurons and opened the door to neuroscience research. Compared to morphology, studying the function and dynamic activity of neurons *in vivo* has been considerably more difficult. Extracellular recordings of neuronal spike patterns and intracellular recordings of membrane potential have been used as main tools to study the *in vivo* activity of the brain for many years. However, simultaneous intracellular recording of the membrane potential dynamics from all the thin and extensive dendrites of a neuron, or from hundreds to thousands of neurons remains an outstanding challenge for neurophysiologists.

Two-photon excited fluorescence laser scanning microscopy (TPLSM), a nonlinear optical microscopy technique, was invented in 1990 to enable the study of neuronal function at the subcellular level *in vivo* [1]. In a quantum event, a fluorophore can absorb

two photons simultaneously if each photon has half of the energy required to excite the fluorophore. A photon with lower energy has longer wavelength and the resulting near-infrared excitation employed in TPLSM (700-1000 nm) causes less scattering and photon damage in the tissue, allowing deeper penetration depth when compared to the confocal microscope (up to 800 μm-1 mm in the neocortex; [2]). Since the fluorescent molecule absorbs two photons simultaneously to reach its excited state, the probability of two-photon absorption is proportional to the square of the incident laser intensity. Therefore, only excitation light within the focal region contributes significantly to the fluorescent signal. This nonlinearity of absorption provides an intrinsic mechanism for optical sectioning by the incident beam. In confocal microscopy, the increase in excitation necessary to compensate for the signal loss caused by rejection of scattered and out-of-focus photons by the detector pinhole further exacerbates photobleaching and photodamage. In contrast, the three-dimensional optical sectioning effect of TPLSM decreases the photobleaching of tissue and avoids the pinhole throughput loss that exists in a confocal laser scanning microscope. Continuous technological developments in recent years have been made to refine the technology of TPLSM, mainly to push limits of the imaging speed, resolution and imaging depth. TPLSM combined with functional markers such as calcium indicators or voltage sensitive dyes provides a powerful tool to study the function and dynamic activity of single neurons or neuron networks *in vivo*.

Although commercial two-photon microscopes are available, there are several advantages in building a custom two-photon microscope. One important advantage is the flexibility to choose all the components of the system including the microscope, scanners and laser, which allows for tailoring of the system to specific purposes. Price is another important consideration. Commercial systems are considerably more expensive than custom-built ones. Most importantly, the process of building a two-photon microscope provides deeper understanding of how the system works, how to maintain it, and how to modify it to interface with other experimental systems.

1.2 The Lobula Giant Movement Detector (LGMD) in locusts

The LGMD neuron is a large visual interneuron located in the third neuropil of the optic lobe of the locusts [3]. The LGMD neuron is most sensitive to objects approaching on a collision course with the animal or their two-dimensional simulations (i.e., looming stimuli; [4], [5], [6]) and plays an important role in visually evoked escape behavior [7], [8]. The LGMD output spikes are coupled 1:1 with those of its postsynaptic target, the descending contralateral movement detector (DCMD). The DCMD neuron has the largest axon in the locust nerve cord and projects to thoracic motor centers where it makes synapses with identified motor and interneurons implicated in the generation of jump and flight [9], [10].

The LGMD neuron has three dendritic fields (A-C), which receive visual input from the entire visual hemifield sampled by the ipsilateral compound eye (Fig. 1). The largest one, called field A, receives ~15,000 retinotopic excitatory inputs, whereas fields B and C receive ~500 nonretinotopic feedforward inhibitory inputs. The inputs to dendritic field A have been shown to activate calcium-permeable nicotinic acetylcholine receptors in reference [11]. This study employed wide-field charge-coupled device (CCD) camera imaging with a relatively low penetration depth and spatial resolution. As a consequence, fine-scale retinotopy was revealed indirectly and the range of questions that could be addressed was limited compared to those that can be addressed with the experimental techniques described here.

2. Materials

2.1 Animal Preparations

Experiments were carried out on mature locusts (mostly female), 3–4 weeks past the final molt, taken from a crowded colony. Animals were mounted dorsal side up on a plastic custom holder and immobilized by wax and vacuum grease. The head was rotated 90° with the anterior side pointing downward. The entire head and neck were bathed in ice-cold locust saline [12], except for the right eye used for visual stimulation. The gut was removed. The head capsule was opened dorso-frontally between the two eyes. The muscles in the head capsule were removed. The cuticle and muscles on the neck were removed as well, leaving only the two nerve cords and four tracheas attached. The right optic lobe was desheathed mechanically with fine forceps. A metal holder coated with wax elevated and stabilized the brain and the right optic lobe.

2.2 Staining

The LGMD was uniquely identified through its characteristic spike pattern in 1:1 correspondence with that of its postsynaptic target, the DCMD, recorded extracellularly from the nerve cord with hook electrodes. At the beginning of an experiment, the LGMD neuron was impaled with a sharp intracellular electrode (230–300 MΩ) containing 3µl of 2 M potassium chloride and 1 µl of the calcium indicator Oregon Green BAPTA-1 (OGB1, hexapotassium salt, 5 mM; Thermo Fisher Scientific, Waltham, MA). Iontophoresis of OGB1 was achieved with current pulses of -3 nA, alternating between 1 s on and 1 s off, that lasted for 6 min. The pulses were delivered by an Axoclamp 2B amplifier (Molecular Devices, Sunnyvale, CA). Intracellular signals were amplified in bridge mode with an Axoclamp 2B and an instrumental amplifier (Brownlee Precision 440; NeuroPhase, Palo Alto, CA). Intracellular LGMD and extracellular DCMD signals were acquired using Scanimage and a data acquisition card with a sampling rate of 0.19 MHz (PCI 6110; National Instruments, Austin, TX).

2.3 Imaging, Single-Facet Stimulation and Electrophysiology

After dissection and staining with OGB1, the animal was moved to the two-photon microscope setup. The excitation wavelength was 820 nm, and the emission filter had a pass band between 500 and 550 nm (ET525/50M-2P; Chroma Technology, Bellow Falls, VT). The single facet stimulation setup was adjusted to focus on the locust right eye. Each single-facet visual stimulus was an "OFF" flash lasting 50 ms subtending a size of 22 μm at the retina and focused at the center of an ommatidium on the compound eye (ommatidium diameter: ~24 μm). The brightness of the display before and after the flash was 72.43 cd/m^2. The brightness of the screen at the level used for "OFF" stimuli was 1.63 cd/m^2. The brightness of the screen was calibrated by a photometer and linearized by loading a normalized gamma table to the MATLAB Psychtoolbox used to generate the stimuli (see below).

Before carrying out single-facet stimulation, we used a larger flash stimulus centered at the same location as the single-facet stimulus to approximately locate the activated dendritic branches on field A of the LGMD. In our experimental configuration, the dendritic branches of field A extend several tens of micrometers along the z-axis of the microscope. Consequently, it is time consuming to find the exact z-plane of the activated branches under two-photon imaging due to its restricted depth of field (~ 2 μm). Instead, we employed the microscope in the single photon CCD mode to obtain a larger depth of field. After finding the activated branches, we switched to the two-photon mode while presenting the single-facet stimuli.

3. Methods

3.1 Building a Custom Two-Photon Microscope

A custom TPLSM is composed of a light source, a beam reshaping and expanding system (consisting of two telescopes), a scanning system, dichroic filters, and a light detection module (Fig. 2). The whole system is laid out on an air table. Our construction detailed below mainly follows the principles exposed in reference [13] with a few modifications to adapt them for our own needs.

3.1.1 Light source

For a continuous-wave laser, the probability of the near-simultaneous absorption (within ~0.5 fs) of two photons by a fluorescent molecule is extremely low. Therefore, a temporally resolved high flux of excitation photons is required, usually from a sub-picosecond pulsed laser. Pulsed lasers are not monochromatic. Shorter pulse widths

corresponds to broader spectral widths according to the formula:

$$\Delta\lambda \sim \frac{{\lambda_0}^2}{c \cdot \tau_{pulse}},$$

where λ_0 is the center wavelength, c is the speed of light and τ_{pulse} is the pulse width. In TPLSM the center wavelength of the laser is typically in the near-infrared range of the electromagnetic spectrum, between 700 and 1000 nm. Commercially available Titanium-sapphire (Ti: Sapphire) systems are capable of generating pulses with a width of 140 fs. The corresponding spectral width is 10-20 nm. This width is narrower than the width of the two-photon absorption band of many dyes. The average output power and the repetition rate of the laser can be monitored by a photodiode and a fast oscilloscope, respectively. A commercial Ti: Sapphire system can provide average laser power up to ~3 W, in a wavelength range of 670-1070 nm with a repetition rate of 80 MHz that matches typical fluorescence lifetimes, thus balancing excitation efficiency and dye saturation [14]. A pulsed Ti: Sapphire laser boosts the two-photon excitation rate 10^5 fold compared to a continuous-wave laser at the same average power.

Ti: Sapphire lasers are linearly polarized. To control the laser power to the two-photon microscope, a half-wave plate mounted on a motorized rotation stage is placed at the laser outlet, which rotates the polarization angle of the laser. A polarized beam splitter is used to separate the s- and p-polarization components by reflecting the s-component and passing the p-component. The s-component is dumped to a beam trap while the p-component is transmitted to the two-photon microscope. To decrease the photodamage caused by the excitation laser, the laser power passed through the objective lens is controlled to be as low as possible (normally below ~100 mW, with penetration of thicker tissue requiring higher power). A large fraction of the laser power is therefore unused and dumped to the beam trap.

3.1.2 Laser Beam Reshaping and Expansion

The optical resolution of a lens follows the Rayleigh criterion:

$$r \sim \frac{0.61 \cdot \lambda}{NA}$$

where r is the minimum distance between resolvable points, λ is the wavelength of light and NA is the numerical aperture of the lens. Because the radial intensity profile of the laser beam is Gaussian, making use of the full numerical aperture of the objective lens to obtain diffraction-limited focusing requires the laser beam diameter to slightly overfill the diameter of its back aperture (D_{BA}), although this decreases slightly the transmitted power. To take a concrete example, in our setup the beam diameter coming from the laser head is about 1.4 mm, and is thus much smaller than D_{BA} (e.g., 18 mm for a 20 X Olympus water dipping objective lens). It is therefore necessary to expand the beam diameter. In addition, due to the limited size of the XY scanning mirrors (~6 mm), using

two beam-expanders is optimal with the first one expanding the beam from 1.4 mm to 6 mm before the mirrors and a second one expanding the beam from 6 mm to 20 mm after the mirrors. There are several ways to expand laser beams, such as the Keplerian (or astronomical) telescope and the Galilean telescope (Fig. 3). The magnification power of both telescopes is the ratio of the focal lengths of their two lenses. $MP=|f_o|/|f_e|$.

3.1.3 Scan System

The objective lens converts a collimated beam into a diffraction-limited focal spot on the focal plane of the objective lens. By using a scan system that changes the angle of incidence of the collimated beam, the focal spot can be moved throughout a desired region of the sample. A standard scan system consists of a scan head, which is typically composed of one or two scan mirrors, a scan lens, a tube lens and an infinity-corrected objective lens (Fig. 4). The selection of the scan lens influences the imaging quality. Off-axis beam deflection by the scan mirrors through a focusing lens generally results in aberrations, with the image spot being mapped onto a curved surface as opposed to a desirable flat plane. In general, to design a simple custom scan lens, a combination of two or three lenses with large diameters and long focal lengths works better than a single lens of the same effective focal length, because each lens in the combination has a larger curvature radius than that of a single lens. For example, in our system a combination of two 2" diameter (Ø) lenses with focal lengths of 150 mm and 200 mm (effective focal length = 60 mm) performs better than a 1" Ø lens with focal length of 60 mm.

Since the size of the scan mirrors is usually smaller than D_{BA}, an appropriate selection of the focal lengths of the scan and tube lenses is required to construct a second telescope system expanding the beam diameter to slightly overfill the back aperture of the objective lens. Two scan mirrors with rotational axes orthogonal to each other are used to generate a simple 2-D scan pattern. When aligning these optical components, the conjugate plane of the back aperture of the objective lens needs to be placed halfway between the two scan mirrors. Among the various types of XY scanner designs currently available, such as resonant scanners, acousto-optical scanners and galvanometric scanners, the most common one is the galvanometric scanner, which scans the focused beam across the sample with an adjustable scan speed, allowing software ‘zoom in’ and rotation of the scan axis. In our current system, we use galvanometric scanners from Cambridge Technololgy (Bedford, MA; model 6215HSM40B). These scanners are capable of rotations of up to ±20º at rates of up to 2 kHz at reduced deflection angles. The aperture size and the scan angle we use are 5 mm and ±5º, respectively. Under a 16 X Nikon objective lens, the deflection of the mirrors corresponds to a distance of 550 μm in the focal plane. The scan head is attached to a 2" Ø post through a custom metal holder and a XY translational stage allowing precise adjustment of the position of the scan head.

3.1.4 Filters and Fluorescence Detection

After passing the scan system, the laser is reflected by a short pass dichroic mirror (see note 1), λ_{cut}=700 nm (mirror 1 in Fig. 5A). The fluorescence signal generated from the sample is emitted over the solid angle of an entire sphere enclosing it (4π). A portion of this fluorescence passes back through the objective lens and is deflected by a second dichroic mirror, which is used to separate excitation and fluorescence, λ_{cut}=560 nm (long pass, mirror 2 in Fig. 5A). It then passes through a band-pass filter and a collection lens to the photomultiplier tube (PMT, H7422P-40; Hamamatsu, Bridgewater, NJ). To optimize the collection efficiency, the back aperture of the objective lens is imaged onto the PMT detection plane. The PMT is placed as close to the objective lens as possible to collect as many scattered photons as possible. The PMT is maintained at a constant temperature by monitoring a thermistor which regulates the current to a thermoelectric cooler housed in the PMT case. The temperature of the PMT outer case rises due to the thermoelectric cooler. A heatsink with a fan is attached to the outer case to prevent a temperature rise in the PMT. The PMT connects to a preamplifier (current-to-voltage conversion, C7319, Hamamatsu) whose output connects to the data acquisition board. It is easy to switch from the two-photon excitation mode to the traditional wide-field epifluorescence excitation mode by changing dichroic mirror 2 with dichroic mirror 3 (long pass, λ_{cut}=505 nm), as illustrated in Fig. 5B. The whole-field fluorescence imaging system is excited by light from a Mercury lamp and the fluorescence is collected by a CCD camera (Rolera XR, QImaging, Surrey, BC, Canada).

3.1.5 Electronics and Software

Each galvanometric scanner mirror is driven by a MicroMax™ Series positioning system (Cambridge Technology) that receives as input an analog ±10 V signal and transforms it into a positioning angle. The scanner electronics and driver boards ensure that the horizontal and vertical scans are synchronized with each other to generate a coherent raster pattern. They are also synchronized with the data acquisition. The MicroMax™ driver boards were mounted on a breadboard (Thorlabs) and connected to the scanner mirrors by electrical cables that were terminated on the connectors supplied by Cambridge Technology using commercially available crimp tools. In addition, as the driver boards generate substantial heat during operation, a custom-made heat sink was connected to each one of them through a thermally conductive phase change sheat (Alpha Novatech and Laird Technologies). The heat sinks allowed mounting of two fans on top of them that were connected to a power supply to enhance cooling (Cofan-USA and Astrodyne). The data acquisition board we use is a standard peripheral component interconnect (PCI) board (model PCI-6110, National Instruments, Austin, TX), which has two 16-bit analog outputs, 8 digital I/O lines and four simultaneously sampled analog inputs with acquisition rate of 5 MS/s. The data acquisition is carried out using the

Matlab-based software Scanimage r 3.8 (Vidrio Technologies, Ashburn, VA). Scanimage controls the PCI board that sends analog inputs to drive the two galvanometric scanning mirrors for two-photon imaging while simultaneously receiving analog inputs from the preamplifier connected to the PMT. Scanimage also controls the motorized micromanipulator MP285 (Sutter) through a serial port for adjusting the XY position of the animal holder and the rotation angle of the step motor that controls the Z-axis position of the objective lens. We ordered from Sutter and installed in the MP285 a microcontroller providing a firmware upgrade (KS3.4) to correctly interface with ScanImage. A custom serial cable was fabricated to connect the MP285 to the XY-motors and the Z-step motor using a wiring diagram provided by Sutter. The step motor was fixed on the air table through a custom holder and connected to the manual fine-adjustment front Z-focus of the microscope via the fast-feed knob provided by Olympus and a flexible shaft coupler. Microlimiting switches can be mounted next to the microscope body to turn off input to the step motor via the serial cable connection and thus limit travel in the Z direction so as not to damage the microscope in case of a mistake by the operator. In practice, experienced operators will not need them. The start of imaging acquisition can be activated by the onset of a stimulus via a trigger input to the PCI board.

3.1.6 Image Resolution

After the TPLSM was constructed, we calibrated the lateral and axial resolution of the image. The resolution of the microscope can be determined by imaging fluorescent yellow-green carboxylate-modified microspheres (Thermo Fisher Scientific, Waltham, MA) whose size (~0.1 μm) is below the optical resolution limit. The beads are suspended in 2% agarose gel for imaging. To assess the imaging quality, a maximum Z-stack projection was formed (Fig. 6). By computing the full-width at half-maximal intensity of individual beads along the lateral and axial axes using a series of images taken at different depths, we determined the lateral and axial resolutions to be 0.5 μm and 2 μm, respectively, for a 0.8 NA, 16X magnification Nikon water dipping objective lens.

3.1.7 Microscope Body

The body of the two-photon microscope is based on the upright Olympus BX51 WI microscope (Fig. 7A). The laser beam that passed through the scanning system and beam expanders enters the microscope from the right through the side input port of a module U-DP that can be purchased from Olympus separately and mounted between the filter turret and the binoculars pieces of the microscope. We drilled four holes in a 30 mm Thorlab cage plate and screwed it to the side input port of the U-DP module. This cage plate was connected to a 30 mm to 60 mm cage adapter. This allowed mounting a 60 mm cage system supported on one side by the U-DP module and on the other side by a 1.5" Ø

post positioned immediately before the scanning mirrors. The cage system facilitated the alignment and mounting of the scan lens and the tube lens. As explained in sect. 3.1.4, two dichroic mirrors are placed inside the microscope. The beam reflects from the first dichroic mirror mounted in the U-DP module using an Olympus filter cube and heads to the objective lens (Fig. 7A). We also mounted in the same filter cube a band pass filter to prevent any accidental propagation of laser light to the eye pieces (Fig. 7A). The PMT is mounted on the left side of the microscope with a collecting lens placed in a cage system just in front of it. To allow light to exit the microsope on the left side, we drilled a hole aligned with the optical path of the microscope and 4 additional threaded holes for fixing the rods of a 30 mm cage system onto the microscope body (Fig. 7A). To reflect the fluorescent beam to the PMT we custom fabricated a filter cube similar to the ones inside the microscope turret, but rotated 90º. The second dichroic mirror was mounted in it. The mercury lamp used for conventional wide-field epifluorescence is located on the back of the microscope. In Fig. 7B, the dashed line shows the light path after switching to wide-field mode. The animal is placed on a custom holder, which is attached to a motorized micromanipulator that controls the X- and Y- axis position of the animal (MP285, Sutter Instruments, Novato, CA). In addition, a X,Y manual translational stage (two linear stages mounted orthogonally, 25 mm travel distances) mounted on a height-adjustable post that attaches to the air table is attached to an aluminum breadboard working as a XY platform. The breadboard is also attached to two additional posts with metal balls (ball transfer units) on top, to allow independent positioning of the breadboard and animal in its holder (Fig. 7).

3.2 Construction of a Single Ommatidium Stimulation Setup

Locusts have compound eyes. Each locust compound eye consists of ~7,500 ommatidia (facets) and receives visual input from an entire visual hemifield. Because the locust eye is of the apposition type [15], each facet represents the elementary sampling unit of the eye and determines its finest level of spatial resolution. To study the detailed structure of the retinotopic mapping onto the LGMD dendrites, we designed an optical setup that delivers spatially resolved visual stimuli to individual facets [16], [17].

Our single-facet stimulation setup lies perpendicular to the objective lens of the two-photon microscope (Fig. 8A). The space between the animal's right eye and the horizontally positioned objective lens (10 X, 0.3 NA, water immersion; CFI Plan Fluor 10XW, Nikon Instruments, Melville, NY) was submerged in water to neutralize the lenses of each ommatidium that have a similar refractive index [18]. The objective lens was focused in the plane of the photoreceptors behind the cornea, visualized with a ring light mounted on the objective (Schott, Southbridge, MA). Visual stimuli were delivered by a miniature organic light-emitting diode (OLED) display (0.5 inch, 800 X 600 pixels, 60 Hz refresh rate; OLiGHTEK SVGA050SG). A pellicle beamsplitter (BS) directs half

of the ring-lamp light reflected from the eye and half of the light from the OLED display towards the CMOS camera sensor where they are both focused by an additional lens, allowing simultaneous visualization of the stimulus and the compound eye. In a sample image taken by the CMOS camera (Fig. 8B), the darker facet at the center is being stimulated with an OFF-stimulus, which subtends a size of 22 μm at the retina. Visual stimuli were generated with the Psychtoolbox and MATLAB (The MathWorks, Natick, MA). By changing the magnification of the horizontal microscope, we can adjust the field of view on the locust eye. One easy way to do so is to use insertable lenses with different focal lengths, which are mounted in lens holders at different distances from the image plane (Fig. 8C). During an experiment, we can first roughly locate the region to be stimulated by using the lower magnification view, and next change to higher magnification when delivering single-facet visual stimuli (Fig. 8D). To stimulate facets at different locations on the eye, the use of a 3 dimensional translational stage (Newport, Irvine, CA) is helpful (Fig. 8C). After moving the visual stimulus to a certain facet of interest, the ring light is turned off to perform two-photon imaging. Because the horizontal objective is a water immersion lens, it is necessary to build a water tight holder around the locust eye (Fig. 8E inset, see note 2). The water holder we built was made of a curved piece of black tape held in place by black wax and sealed with vacuum grease. This water holder also blocked most of the light from the visual display that was otherwise able to propagate through the vertical objective lens of the two-photon microscope and therefore reduced the background noise.

3.3 Detailed Structure of the Retinotopic Mapping

We first acquired a low magnification image of dendritic field A (Fig. 9A, top). In response to a single-facet stimulus, several dendritic branches within the yellow rectangle were activated (Fig. 9A, top). On average, we found that ~4 distinct dendritic branches were activated by single-facet stimulation. We then focused on specific dendritic segments that were activated by the stimulus (Fig. 9A, bottom left). The relative fluorescence change was computed as $dF/F=(F(t)-F_0)/ F_0$, where F_0 is the baseline fluorescence computed as the average of the first five frames before the stimulus and the last five frames of the recording. To obtain the spatial distribution of the relative fluorescence change, and its evolution with time (Fig. 9B), we segmented each branch in 2-μm-wide strips and computed the average relative fluorescence change within each sequential strip (Fig. 9A, bottom right). On some branches, the peak amplitude of dF/F was much stronger than on others (Fig. 9B). On the same branch, different locations could have large differences in the amplitudes of dF/F (Fig. 9C). One possible cause for the differences in the amplitudes of relative fluorescence change at different locations is the diffusion of calcium from a single entry point along the branch. To address this issue, we examined the time evolution of the dF/F along a single branch. After normalizing each curve to it peak value, we detected almost no change over time in the shape of the

spatial dF/F distribution. (Fig. 9D). This is not expected from diffusion of calcium over the same distance [19].

Next, we delivered visual stimuli to adjacent facets and studied their spatial activation pattern on the LGMD dendrites. Three single-facet stimuli were presented along either the anterior-posterior axis or the dorsal-ventral axis (Fig. 10A, 10B). We found as noted above that stimulating one facet activated more than one dendritic branch. In addition, stimulating adjacent facets resulted in overlapped activation patterns on the same dendritic branches. We computed the center-of-mass (COM) of the activated dendritic branches for each facet and plotted its location together with the activated dendritic regions (Fig. 10C, 10D). When plotting the COMs stimulated by three successive facets along the posterior-anterior axis, we found that they were mapped in the same order along the medial-lateral axis of the LGMD dendrite (Fig. 10E). Similarly, the dorsal-ventral axis on the eye mapped to the dorsal-ventral dendritic axis (Fig. 10F). Thus, the projection from adjacent facets to the LGMD excitatory dendrites preserved retinotopy.

As summarized above, we have shown that stimulating adjacent facets activated overlapping excitatory dendritic branches (Fig. 10C, 10D). Do adjacent facets share common synapses or do they make independent synapses over the overlapping dendritic region? To address the question, we took advantage of the fact that the excitatory inputs on dendritic field A activated by small visual stimuli (5°) habituate strongly in response to repeated stimulation, and this habituation is most likely to be located at the presynaptic terminal of the LGMD [20]. Therefore, if the same synaptic input is stimulated in rapid succession, the second stimulation is expected to elicit a weaker calcium response. If two facets share common synaptic input we would expect that stimulating the second facet results in weaker calcium signals after stimulating the first one. Conversely, if the two facets make independent synaptic inputs, then stimulation of the second facet should not dependent on the prior stimulation of the first facet.

In the following experiments, we thus focused on common dendritic branches activated by two adjacent facets. We stimulated each facet twice with an interval of 1 s between stimuli (Fig. 11A, B) and compared the responses to those elicited by stimulating either facet followed by the other one (Fig. 11C, D). The same experiment was repeated with 0.2 s and 0.5 s interstimulus intervals. We compute a paired-pulse peak response ratio P2/P1 (Fig. 11E) to compare the response to the second pulse (P2) with the first pulse (P1, Fig. 11D). In comparison to the responses to sequential stimulation of the same facet, we found that paired-pulse ratios increased with the interstimulus interval, as expected from habituation of synaptic responses (Fig. 11E, Ea-a). We found that at all three intervals of 0.2, 0.5 and 1 s, paired-pulse ratios of the two-facet stimulation protocol (Ea-b) were significantly higher (Fig. 11E, Ea-b). In addition, the paired-pulse ratios did not increase

with increasing interstimulus interval. Taken together, these results suggest that different facets make independent synapses onto the excitatory dendrite of the LGMD.

3.4 Checklist: parts and vendors for the TPLSM and single-facet stimulation setup

Mechanical:

Anti-vibration air table: 4 ft (width) x 6 ft (length) x 8" (thickness), 783 series, TMC (Technical Manifacturing Corp)
Microscope body: Olympus BX51 WI microscope
Mirror mounts: 1" Ø precision kinematic mirror mounts with 3 adjusters for ±4º pitch and yaw adjustment, Thorlabs, Newton, NJ
Posts and clamping forks for posts: mirrors were attached to 1/2" Ø posts. Cage systems and scan head were attached to 1.5" Ø posts from Thorlabs
The aluminum breadboard used as XY platform for mounting the animal holder and other equipment was attached to the air table via two ball transfer units mounted on 2" Ø posts and a XY translational stage controlling a post of adjustable heights (BLP01, Thorlabs).
Dimensions: 18" x 24" x 1/2" (Thorlabs)
Ball transfer units: SMC 1/4, load capacity of 75 lbs, Ball Transfer Systems, LLC, Perryopolis, PA
Assembly rods: 6 mm Ø ER assembly rods for 30 mm and 60 mm cage systems for mounting lenses of beam expanders, Thorlabs
Translational stages: XY translational stage for mounting the breadboard/scan head are composed of two orthogonally mounted linear translational stages, 25 mm travel distance, Thorlabs. The 3-dimensional translational stage for the single-facet stimulation setup, was model 562-XYZ, 13 mm travel distance, Newport, Irvine, CA

Optical:

Ti-Sapphire laser: average power >2.5W, 690-1020 nm, 80MHz repetition rate, Chameleon Ultra, Coherent, Santa Clara, CA
Mirrors: silver coated, λ/10 flatness, Thorlabs
Lenses: achromatic doublets, anti-reflective coating for 650-1050 nm, 1" or 2" Ø, Thorlabs
Dichoic mirrors: long pass dichroic T560lpxrxt (λ_{cut}=560 nm), short pass dichroic T700DCSPXR (λ_{cut}=700 nm), long pass dichroic 41001 (λ_{cut}=505 nm), Chroma Technology Corp, Bellows Falls, VT
Objective lenses: for single-facet stimulation (0.3 NA, CFI Plan Fluor, 10XW), for two-photon imaging (0.8 NA, CFI75, 16XW), Nikon Instruments, Melville, NY
Custom scan lens: two lenses with focal lengths of f=100 mm and f=150 mm (2" Ø achromatic doublets, AR coating: 650-1050 nm) are mounted in a SM2 lens tube, Thorlabs

Wave plate: 1/2" Ø mounted achromatic half-wave plate, 690-1200 nm, Thorlabs
Polarized beam splitter: broadband polarizing cube beamsplitter, 25.4 mm, 620-1000 nm, 10FC16PB.5, Newport
Pellicle beam splitter: cube-mounted, CM1-BP145B1, Thorlabs
Scanners: 6215HSM40B, Cambridge Technololgy, Bedford, MA
OLED display: SVGA050SG, 0.5 inch, 800 X 600 pixels, 60 Hz refresh rate, OLiGHTEK, Yunnan, China

Electronics
Motorized rotation stage (for mounting the wave plate): PRM1Z8, Thorlabs
Step motor: 2-phase, 1.8° (step angle), PK266-01A, Oriental Motor, Torrance, CA
Motorized micromanipulator for controlling the XY motion of the animal holder and rotation of the step motor that controls the Z-axis motion of the objective lens: MP285, Sutter Instruments, Novato, CA, with KS3.4 firmware upgrade.
Data acquisition board: PCI-6110, National Instruments, Austin, TX
Photomultiplier tube (PMT): H7422P-40, sensitive range 300-720 nm; Temperature control and power supply for the PMT: C8137-02, Hamamatsu, Bridgewater, NJ
Preamplifier for the PMT: current-to-voltage conversion, C7319, Hamamatsu. Input voltage to the preamplifier is provided by a DC power supply, E3630, Agilent, Santa Clara, CA

Miscellanous
Power supplies: Astrodyne SP-240-24 (one for each MicroMax^{TM} driver), Astrodyne ESCC-1502 (for the 4 driver cooling fans)
Heatsink: UB13070-25BM (Alpha Co., Japan)
Driver cooling fans: F-6025H12B-R, Co-FAN USA
Coupler for step motor: Helical Products Co, DSAC-100-11-8
Thermally conductive phase change film: T-pcm905C, 102 x 63.5 mm (Laird Technologies)
Crimp tools: Molex 63811-7000, 63811-8700
Microlimiting switches: 311SX3-T (Honeywell)

MP285 (Sutter) DB25 wiring
(i) Output to motors. Ground: Pins 3, 7, 11, 17, 25; Power XB: 4; Power XA: 16; Power YB: 8; Power YA: 20; Power ZB: 12; Power ZA: 24.
(ii) Sensors to input: end of travel switch data, optical left (OPTL) and right (OPTR). X-OPTL: 14; X-OPTR: 2; Y-OPTL: 18; Y-OPTR: 6; Z-OPTL: 22; Z-OPTR: 10.
(iii) Power. +5VDC: 15, 19, 23; GND: 1, 5, 9.

4. Notes

(1) The flatness of the dichroic mirrors used in the optical path of the laser is extremely important for the reflected wavefront. If the mirror is not sufficiently flat, it may cause 'defocusing' or other aberrations such as astigmatism to the reflected beam, although the transmitted wavefront is often not affected. The manner in which a dichroic mirror is mounted will affects its flatness. Mounting using metal clips is not as good a choice for a thin dichroic mirror (<2mm) as properly gluing it to a holder, since the heterogeneous torque stress caused by the clips can severely affect the flatness, which deteriorates the two-photon imaging quality. When we first built our two-photon setup, we failed to realize that it was the mounting of the dichroic mirror by metal clips that caused a weird shape of the point spread function. To debug the problem, we diverted the beam at different locations on the beam path by placing a mirror on the beam path, fed the reflected beam to a lens with a long focal length (f=400mm) and focused the beam onto the sensor of a CCD camera mounted on a motorized linear translational stage. The motorized stage allowed us to move the CCD camera slightly in and out of focus to check the shape of the focal spot. Eventually, we found a weird shape of focal spot only at locations right after one dichroic mirror, which was mounted by means of metal clips. Changing the dichroic mirror with one glued to a holder solved the problem.

(2) The shape of the water surface in the water cap between the locust eye and the horizontal objective lens affects the refraction of light. During an experiment, leakage or evaporation of water could change the stimulation location on the eye. Therefore, it is necessary to check whether the stimulus remains focused onto the same facet from time to time.

5. Conclusions

Two-photon microscopy provides high spatial resolution for *in vivo* experiments, in spite of tiny motion artifacts that often occur during live imaging. It also penetrates deeper, and causes less photo-damage than confocal microscopy. The design and construction of a custom two-photon microscope not only helps better understand the principles of two-photon microscopy but also enables further modifications and improvements to the system to adapt to more complex experimental requirements. Single-facet stimulation allows to accurately probe the visual system at the native spatial resolution of the locust compound eye. In conjunction with two-photon calcium imaging, single-facet stimulation proved to be a powerful tool to dissect the fine structure of the retinotopic mapping from the locust eye onto the excitatory dendrite of the LGMD, as well as the dynamics of calcium signals in response to time-varying visual stimuli. In particular, they revealed the overlapped but independent wiring scheme of adjacent facets onto LGMD dendrites. This detailed description is necessary to accurately model the mechanisms of synaptic integration within the LGMD and better understand the dendritic computations carried out by this neuron. These tools could also be applied to study other visual neurons in the

locust and the visual system of other animals with compound eyes, such as the fly, honeybee, or dragonfly, for instance.

Acknowledgements

References

1. Denk W, Strickler JH, Webb WW (1990) Two-photon laser scanning fluorescence microscopy. Science 248: 73-76

2. Theer P, Hasan MT, Denk W (2003) Two-photon imaging to a depth of 1000 μm in living brains by use of a $Ti:Al_2O_3$ regenerative amplifier. Optics Letters 28: 1022-1024

3. O'Shea M, Williams JL (1974) The anatomy and output connection of a locust visual interneurone: the lobular giant movement detector (LGMD) neurone. J Comp Physiol 91: 257–266

4. Rind FC, Simmons PJ (1992) Orthopteran DCMD neuron: a reevaluation of responsesto moving objects. I. Selective responses to approaching objects. J Neurophysiol 68: 1654–1666

5. Hatsopoulos N, Gabbiani F, Laurent G (1995) Elementary computation of objectapproach by a wide-field visual neuron. Science 270: 1000–1003

6. Schlotterer GR (1977) Response of the locust descending movement detector neuron to rapidly approaching and withdrawing visual stimuli. Can J Zool 55:1372–1376

7. Fotowat H, Gabbiani F (2011) Collision detection as a model for sensory-motorintegration. Annu Rev Neurosci 34: 1–19

8. Santer RD, Rind FC, Stafford R, Simmons PJ (2006) Role of an identified looming-sensitive neuron in triggering a flying locust's escape. J Neurophysiol 95: 3391–3400

9. Burrows M, Rowell CH (1973) Connections between descending visual interneurons and metathoracic motoneurons in the locust. J Comp Physiol 85:221–234

10. O'Shea M, Rowell CH, Williams J (1974) The Anatomy of a Locust Visual Interneurone; the Descending Contralateral Movement Detector. J Exp Biol 60: 1-12

11. Peron SP, Jones PW, Gabbiani F (2009) Precise subcellular input retinotopy and its computational consequences in an identified visual interneuron. Neuron 63: 830–842

12. Laurent G, and Davidowitz H (1994). Encoding of olfactory information with oscillating neural assemblies. Science 265: 1872–1875

13. Tsai PS, Nishimura N, Yoder EJ, DoInick EM, White GA, Kleinfeld D (2002) Principles, design, and construction of a two-photon laser-scanning microscope for *in vitro* and *in vivo* brain imaging. In: *In vivo* optical imaging of brain function, edited by Ron D. Frostig. CRC Press

14. Helmchen F, Denk W (2005) Deep tissue two-photon microscopy. Nature Methods 2: 932-940

15. Shaw SR (1969) Optics of arthropod compound eye. Science 164: 88–90

16. Zhu Y, Gabbiani F (2016) Fine and distributed subcellular retinotopy of excitatory inputs to the dendritic tree of a collision-detecting neuron. J Neurophysiol 115: 3101-3112

17. Jones PW, Gabbiani F (2010) Synchronized neural input shapes stimulus selectivityin a collision-detecting neuron. Curr Biol 20: 2052–2057

18. Franceschini N, Kirschfeld K (1971) Pseudopupil phenomena in the compound eye of Drosophila. Kybernetik 9: 159–182

19. Helmchen F, Nägerl UV (2016) Biochemical compartmentalization in dendrites. In: Dendrites (3rd ed.), edited by Stuart G, Spruston N, Häuser M. Oxford, UK: Oxford Univ. Press

20. O'Shea M, Rowell CH (1976) The neuronal basis of a sensory analyser, the acridid movement detector system. II. Response decrement, convergence, and the nature of the excitatory afferents to the fan-like dendrites of the LGMD. J Exp Biol 65: 289–308

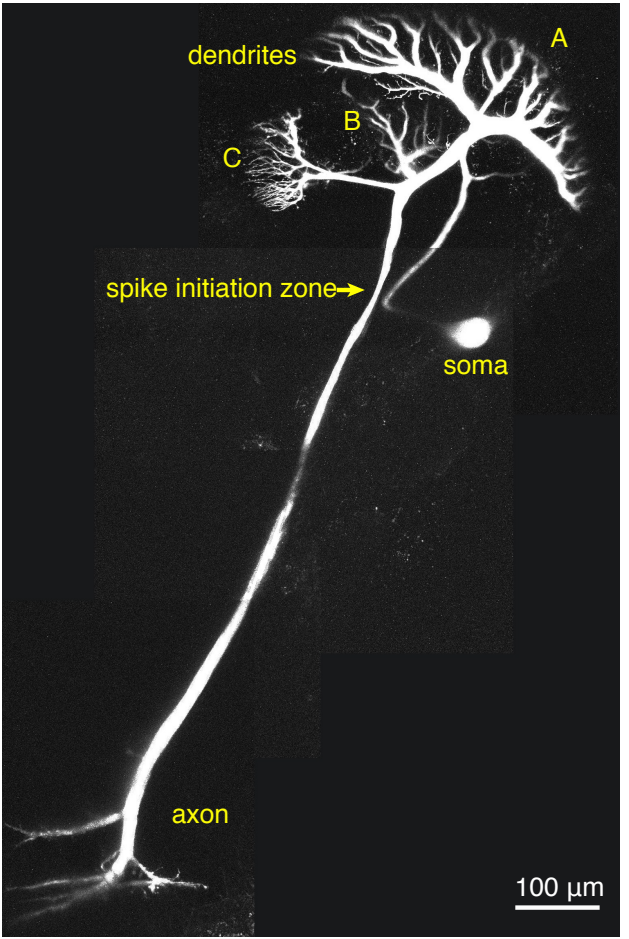

Zhu and Gabbiani, Figure 1

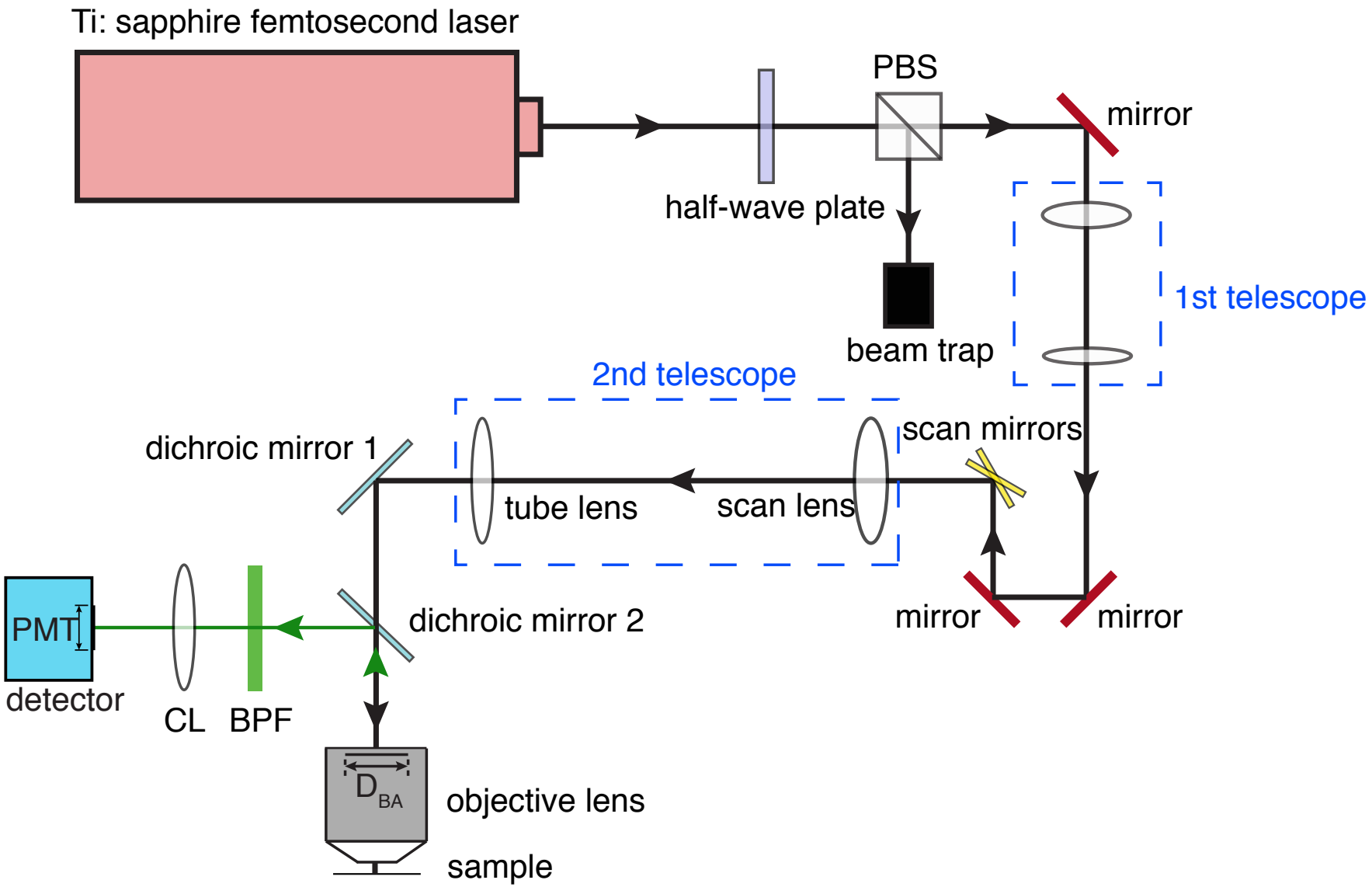

Zhu and Gabbiani, Figure 2

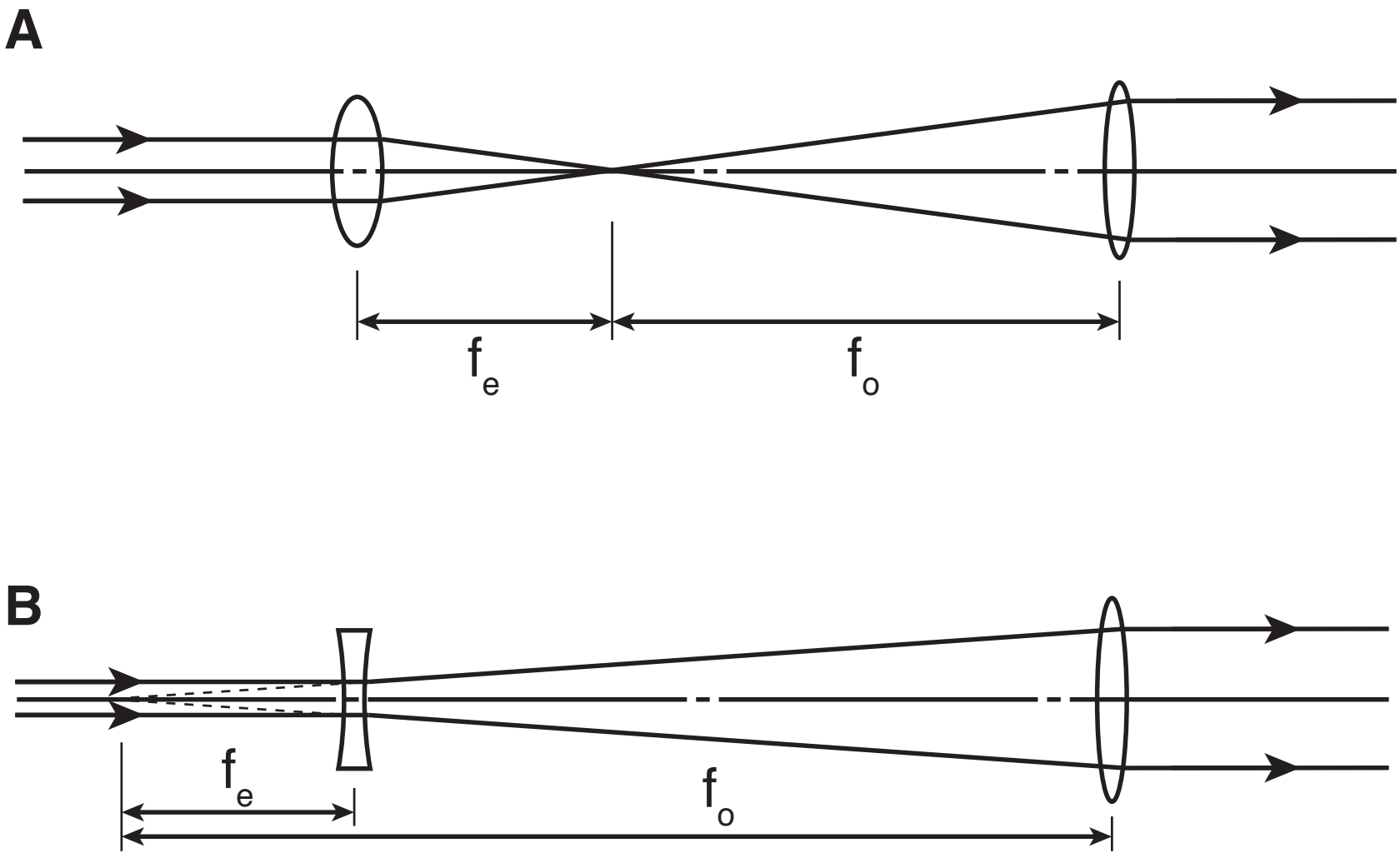

Zhu and Gabbiani, Figure 3

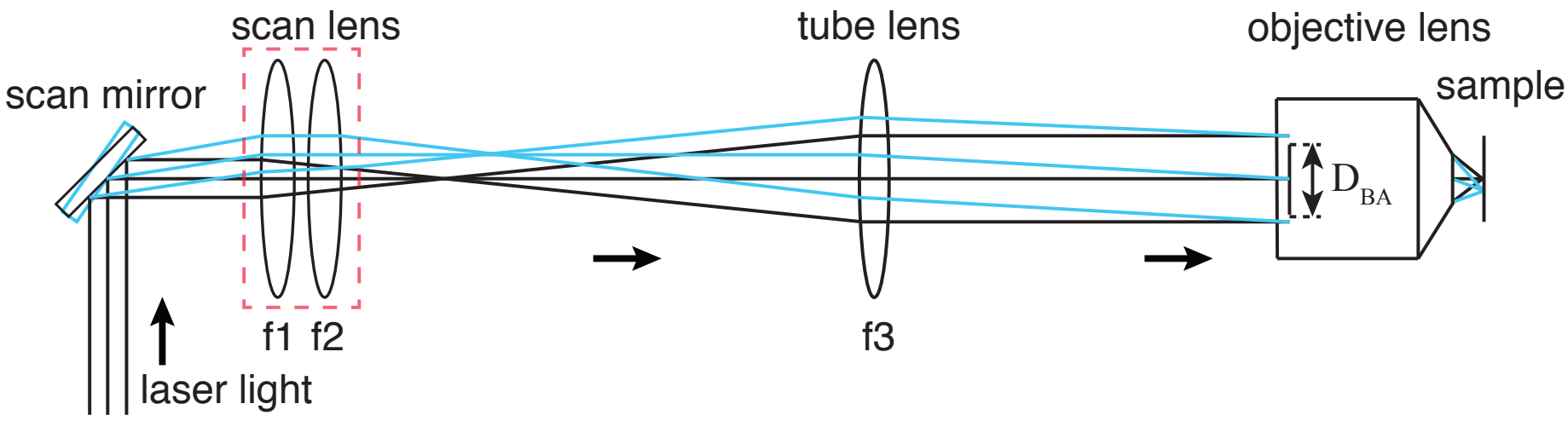

Zhu and Gabbiani, Figure 4

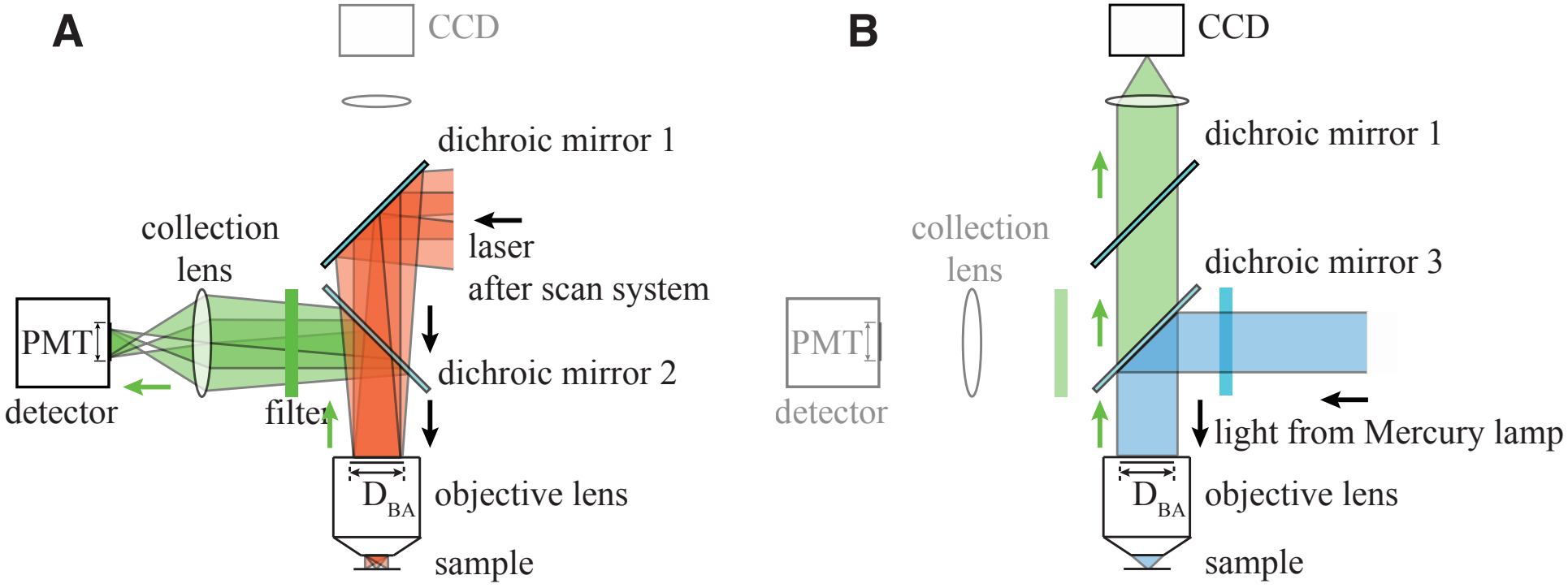

Zhu and Gabbiani, Figure 5

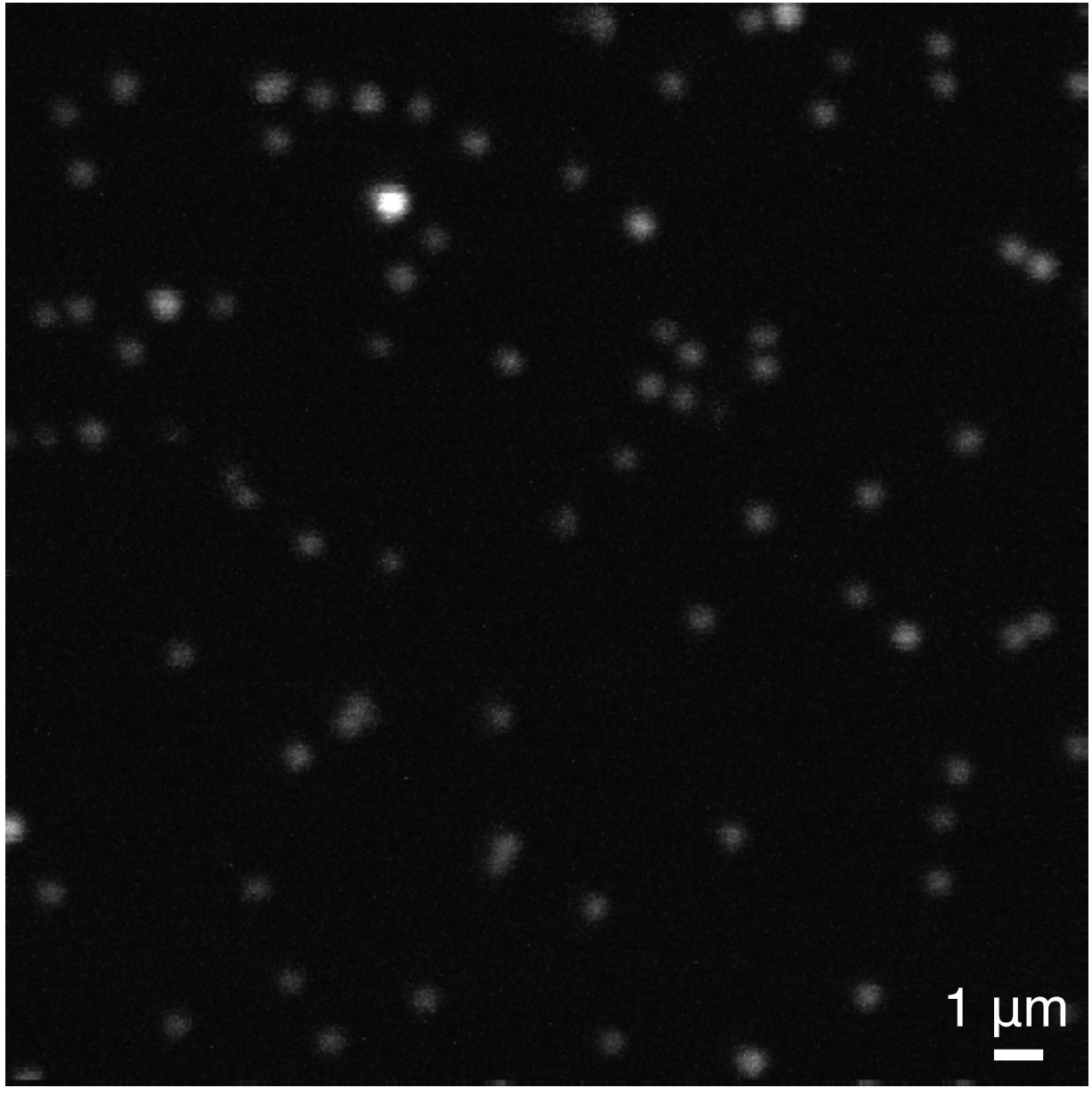

Zhu and Gabbiani, Figure 6

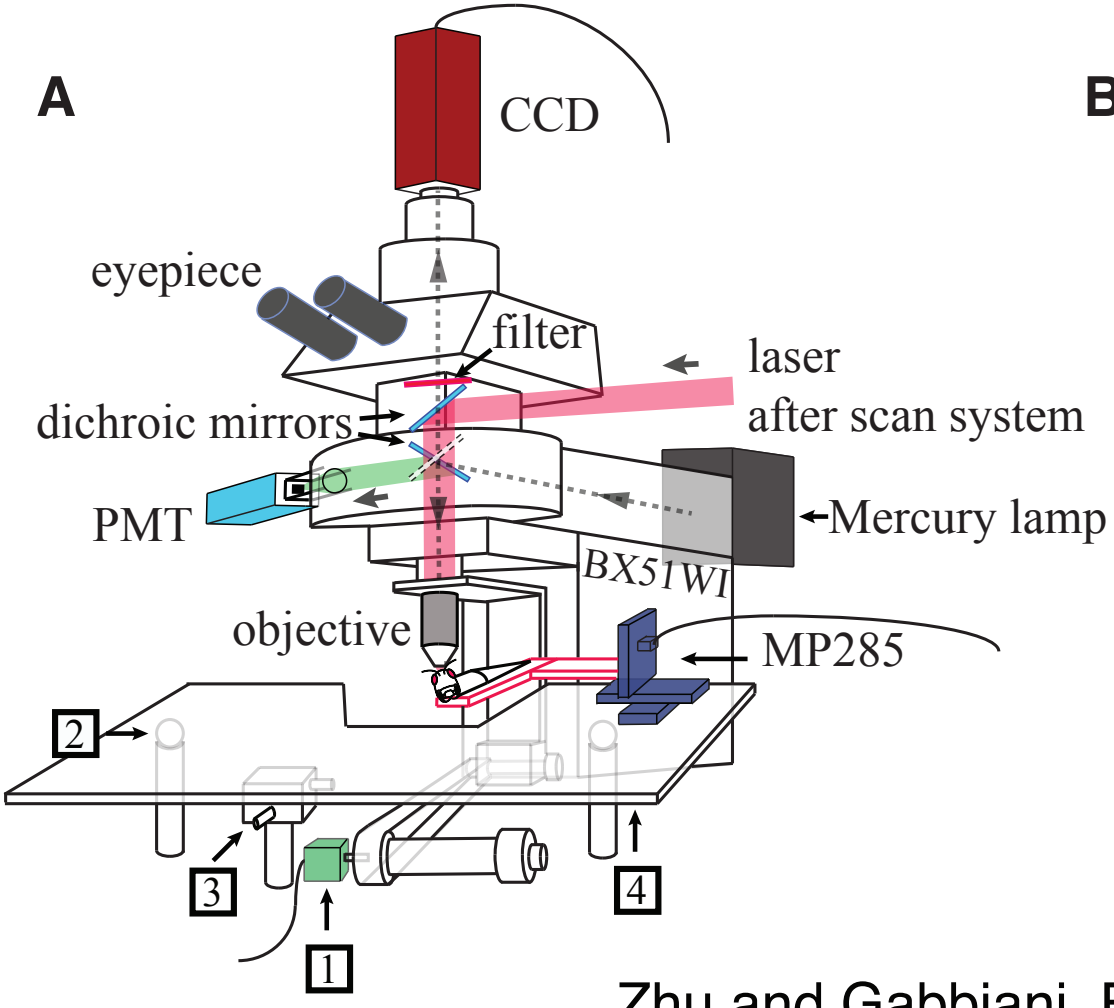

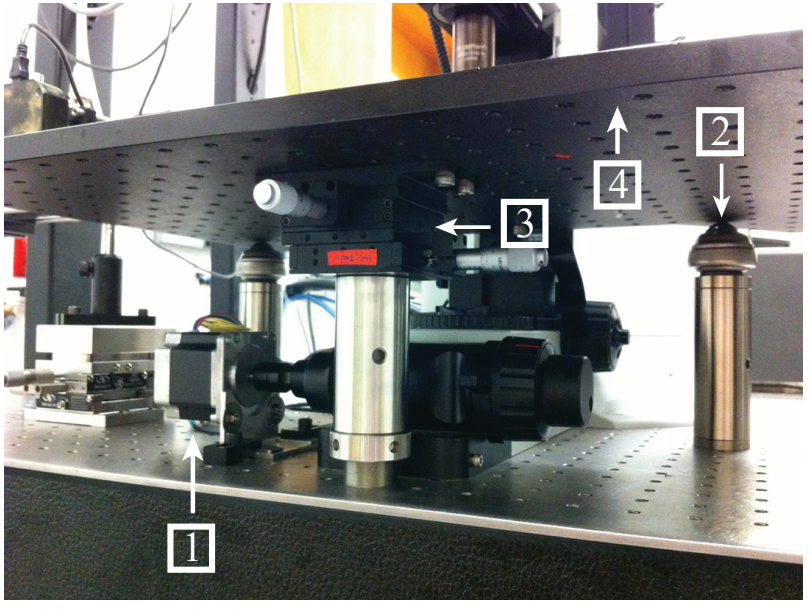

Zhu and Gabbiani, Figure 7

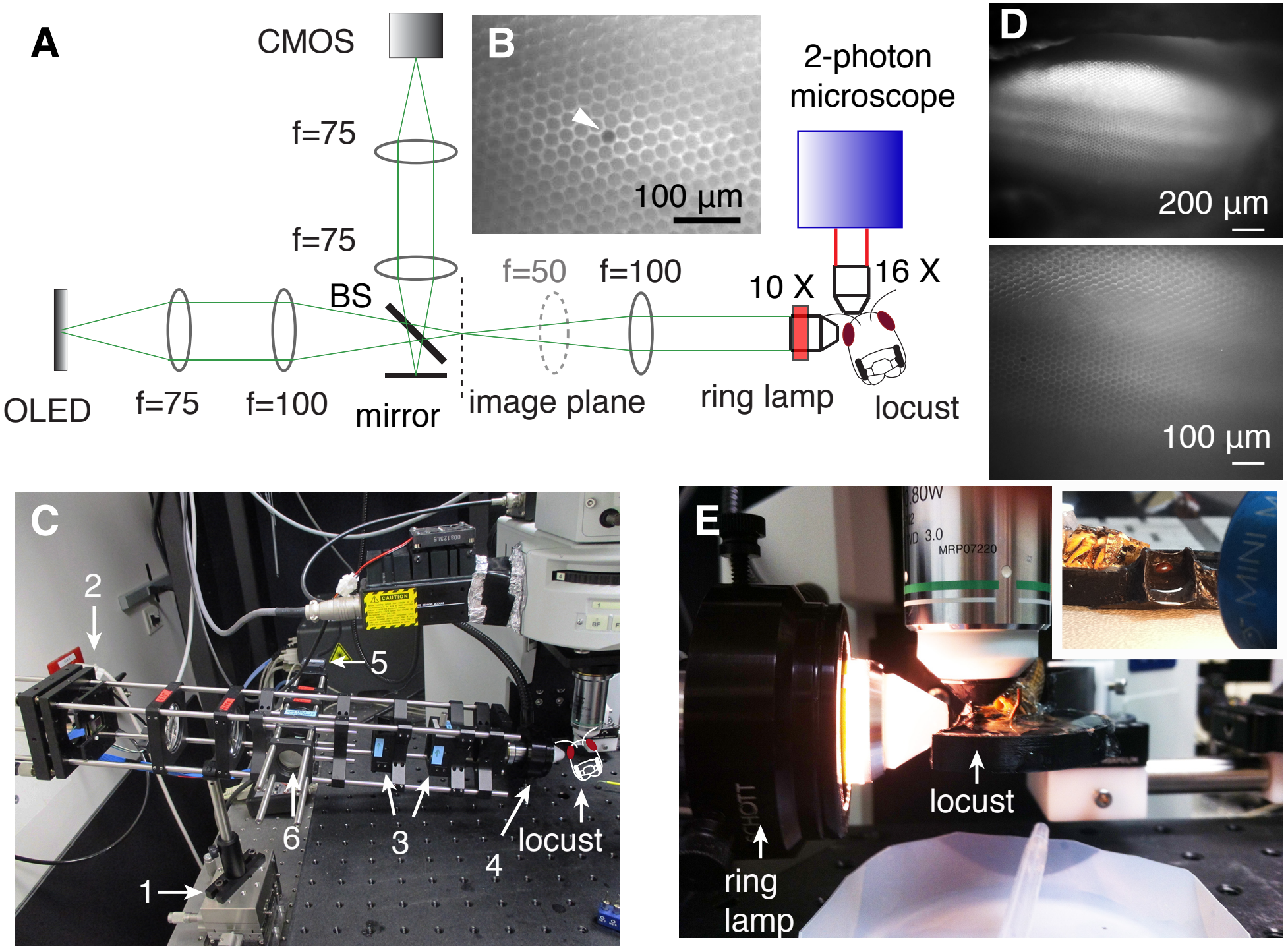

Zhu and Gabbiani, Figure 8

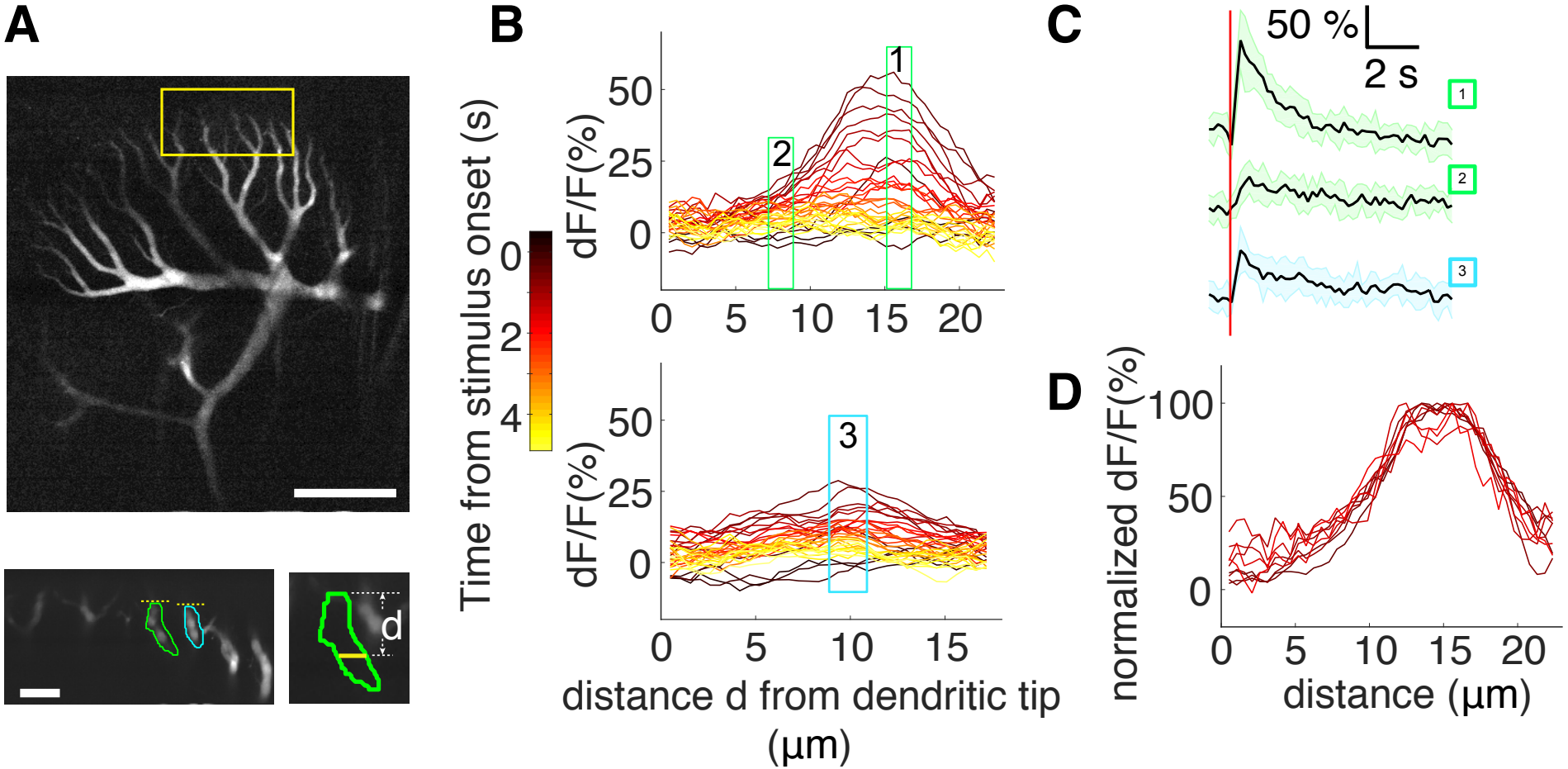

Zhu and Gabbiani, Figure 9

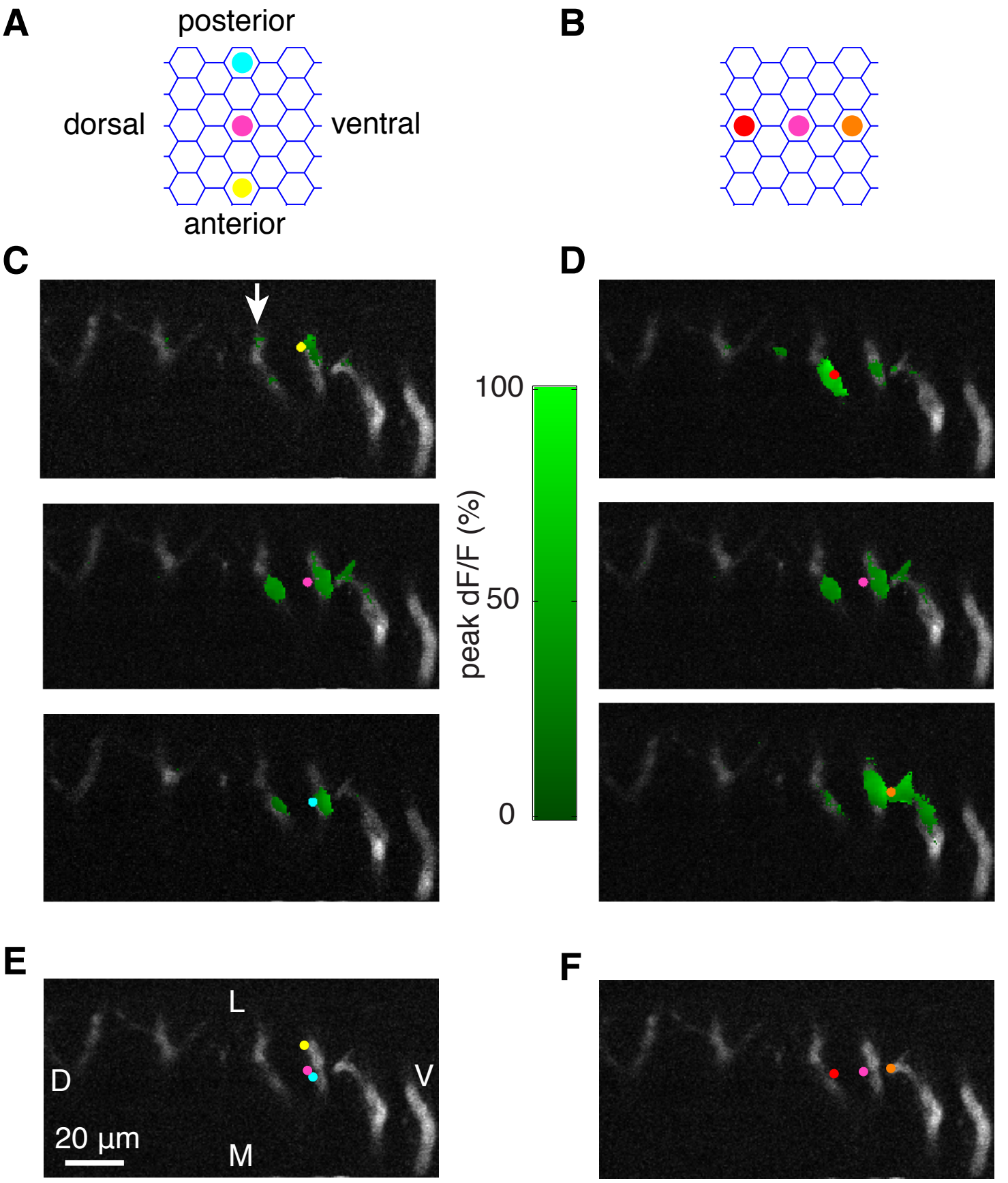

Zhu and Gabbiani, Figure 10

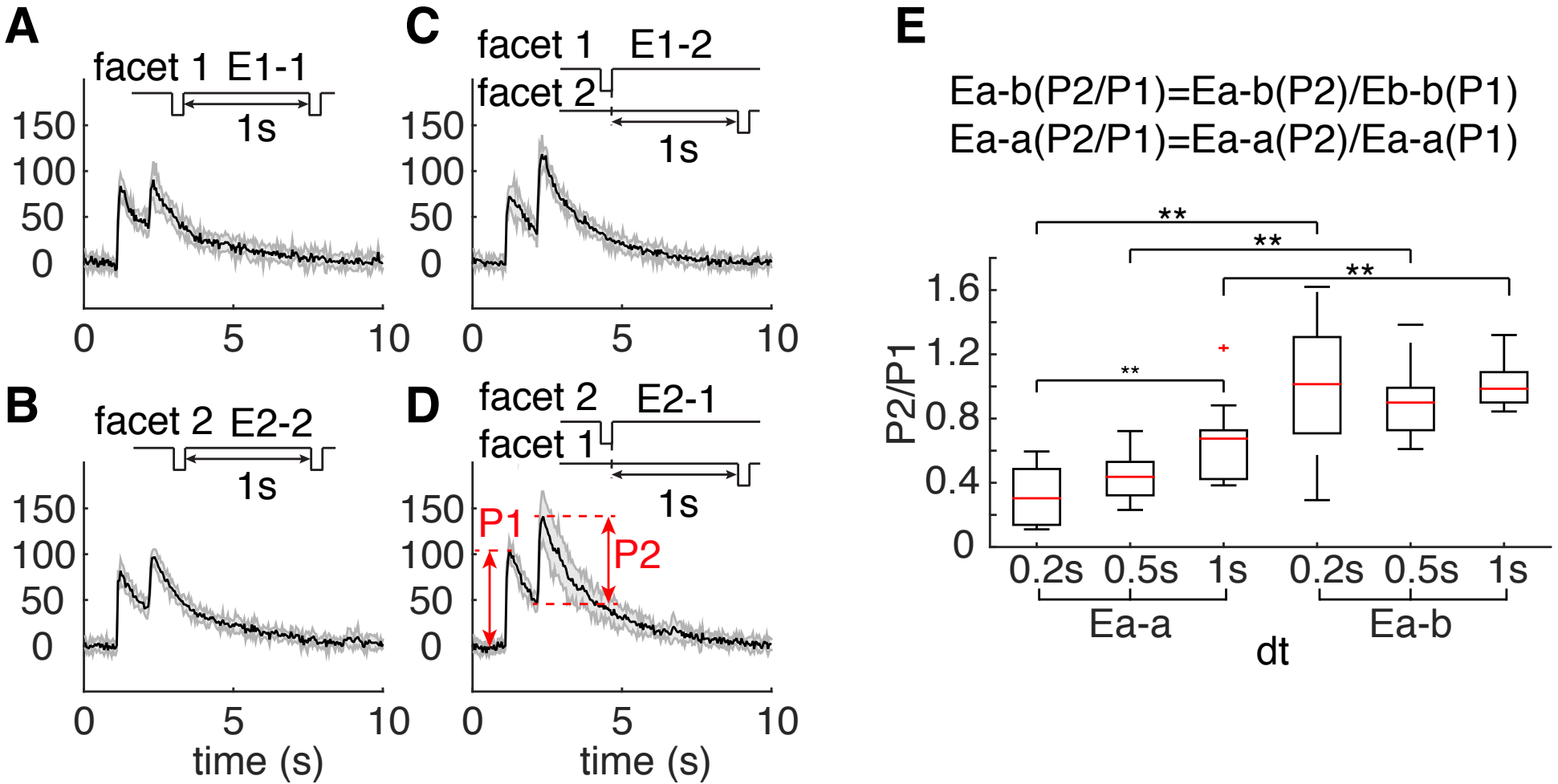

Zhu and Gabbiani, Figure 11

Figure legends

Fig. 1. Two-photon micrograph of an entire LGMD neuron stained with OGB1. The micrograph was obtained by stitching together 4 images of different parts of the LGMD neuron. Each of the constituent images was obtained in turn by maximal projection of a Z-stack of images. The labels A, B and C denote the three dendritic fields of the LGMD.

Fig. 2. Schematics of the configuration of a two-photon microscope. The solid black line indicates the laser beam path, with its propagation direction indicated by the black arrowheads. The solid green line indicates the beam path of the fluorescence signal, with its propagation direction indicated by the green arrowheads Two telescopes are outlined by the blue dashed rectangles. The 'Scan mirrors' in yellow indicates two scan mirrors with orthogonal rotational axes. PBS, polarized beam splitter; BPF, band-pass filter; CL, collection lens; PMT, photomultiplier tube; D_{BA}, diameter of the objective lens back aperture.

Fig. 3. Two basic types of telescopes. The separation between the two lenses is the algebraic sum of two focal lengths f_o and f_e. The magnification is MP = $|f_o|$ / $|f_e|$. **(A)** A Keplerian telescope. In this case f_o and f_e are positive. **(B)** A Galilean telescope. Here f_e is negative and f_o is positive.

Fig. 4. The optical alignment of a scan system. The scan system consists of a scan mirror, a scan lens, a tube lens and an infinity-corrected objective lens. Black and blue lines indicate the laser path corresponding to the scan mirror at the black and blue positions, respectively. The scan lens consists of two lenses with focal lengths f1=150 mm, f2=100 mm. The tube lens has a focal length f3=250 mm. The pivot point of the scan mirror is imaged onto the center of the back aperture of the objective lens. The scan lens together with tube lens also works as a telescope (beam expander).

Fig. 5. Fluorescence detection optics. **(A)** Detection optics for two-photon excited fluorescence. For three different scanning angles, the excitation laser beams are shown in different hues of red, and the emission beams in different hues of green. The back aperture of the objective lens is focused onto the sensor plane of the PMT. **(B)** Detection optics for traditional wide-field excited fluorescence. Light from a Mercury lamp is reflected by the dichroic mirror 3 and excites the sample. The emission beam passes through two dichroic mirrors and is focused onto a CCD.

Fig. 6. Maximal z-projected image of fluorescent microspheres used to calibrate the resolution of our two-photon laser-scanning microscope. The microspheres are 0.1 μm in diameter (Thermo Fisher Scientific, Waltham, MA).

Fig. 7. Realization of the body part of the two-photon microscope. **(A)** Schematics of the microscope body modified from an upright Olympus BX51WI microscope. The two-photon excitation laser beam and emission beam are shown in red and green, respectively. Light coming from the mercury lamp is reflected by a different dichroic mirror (dashed) and its optical path is indicated by the gray dashed line. A band pass filter (BG39, Schott

Corp.) indicated in red on the emission path is used to prevent excessive laser light transmission to the eyepieces. A locust under the objective is fixed on an animal holder, which is attached to a motorized micromanipulator (MP285). (1)-(4) are labeling the same objects in (A) and (B). (1) a step motor; (2) posts with metal balls on top; (3) a XY translational stage on a post attached to the table; (4) aluminum breadboard plate. **(B)** Image of a part of the two-photon microscope body.

Fig. 8. The single-facet stimulation setup. **(A)** Schematics of a single-facet stimulation setup. The focal length of different lenses is denoted by f and their units are in mm. The f=100 mm lens before the 10X objective can be replaced with a f=50 mm lens (dashed lines) to decrease magnification. **(B)** A single-facet off visual stimulus (dark) at the center of the locust eye is marked by a white arrow. **(C)** Realization of single facet stimulation setup. The numbers denote different components of the system: 1, a 3D translational stage; 2, an OLED display; 3, An insertable lens mount on one of two lens holders; 4; a ring light mounted on the 10X objective lens; 5, A CMOS camera; and 6, a mirror. **(D)** Images of the locust compound eye taken by the CMOS camera. Upper panel, lower magnification image using the f=50 mm lens before the 10X objective in (A). Lower panel, higher magnification image using the f=100 mm lens before the 10X objective in (A). **(E)** The positioning of the locust between two objectives. The locust after dissection and staining was fixed on a black plastic holder immersed in locust saline. The ring light on the 10X objective was turned on. Inset, a black water holder surrounding the locust eye was made of black tapes and sealed by black wax and grease. The eye may be seen inside the holder.

Fig. 9. Calcium responses in the LGMD's excitatory dendrite in response to single-facet stimuli. **(A)** top, image of a LGMD neuron filled with OGB1. The yellow rectangle indicates the region that contains the dendritic branches generating calcium responses to single-facet stimuli (50 ms OFF flash), scale bar, 100 μm. Bottom left, expanded view of the dendritic branches in the yellow rectangle that were selected for further analysis in (B)-(D) (outlined in green and blue), scale bar, 20 μm. Bottom right, the average dF/F was computed in each successive 2μm -wide strip (indicated by yellow line) starting from the distal tip of each dendritic branch. d denotes the distance from the center of each strip to the dendritic branch tip. **(B)** Spatial distribution of the average dF/F in each successive 2μm-wide strip along the branches outlined in green and blue, respectively, in (A). Different colors represent different times after the onset of the stimulus. The time courses of dF/F within the green and cyan rectangles are illustrated in (C). (C) Time course of the average dF/F within the green rectangles (1 and 2) and within the cyan rectangle (3) in (B). Black curve, mean of 10 trials; cyan and green shading, standard deviation. Red vertical line denotes the flash stimulus of 50-ms duration. **(D)** Normalized spatial distribution of the average dF/F in each successive 2 μm -wide strip along the branches outlined in green in (A). Each trace is normalized to the peak. The darkest red trace and the lightest red trace are at 0.4 s and 1.7 s after the onset of the stimuli, respectively. Adapted from ref. [16].

Fig. 10. Detailed structure of the retinotopic map on the LGMD excitatory dendrites. **(A)** drawing illustrating the relative position of 3 single-facet stimuli along the anterior-

posterior (A-P) eye axis (each stimulus is a 50-ms OFF flash). **(B)** similar schematics of 3 single-facet stimuli along the dorsal-ventral (D-V) axis (50-ms OFF flashes). **(C)** each panel illustrates the response to a single-facet stimulus along the A-P axis. From top to bottom: anterior, medial, and posterior stimuli, as illustrated in (A). The intensity of green shading indicates for each pixel the peak dF/F amplitude at the corresponding dendritic location. In the top panel, note the slight activation of the branch immediately to the left of the dendritic branch with the strongest response (arrow). The small round spots, color-coded as the stimuli in A, represent the centers of mass (COMs) of the peak dF/F across all pixels. **(D)** Peak dF/F in response to 3 single-facet stimuli along the D-V axis as illustrated in (B). Same plotting conventions as in (C). **(E)** COM of peak dF/F responses for the 3 single-facet stimuli along the A-P axis, replotted from (C). D, dorsal; V, ventral; M, medial; L, lateral. **(F)** COM of peak dF/F responses for the 3 single-facet stimuli along the D-V axis, replotted from (D). Adapted from ref. [16].

Fig. 11. Calcium signals are consistent with different facets making independent synapses onto the same dendritic branch. **(A)** and **(B)**, responses to 2 single-facet stimuli separated by a time interval of 1 s at 2 adjacent facets 1 and 2, respectively. **(C)** and **(D)**, sequential stimulation at facet 1 followed by facet 2 (C) or at facet 2 followed by facet 1 (D) with an interval of 1 s. In (D), the amplitudes of the 1st and 2nd peaks are marked in red as P1 and P2. In (A)–(D), the time courses of average dF/F are taken from the portion of the dendritic branch activated by both facets 1 and 2. Black curves are means of 5 trials; gray shades are standard deviations of 5 trials. Insets are stimulation protocols. **(E)** the ratio of the 2nd peak to the 1st peak either in the protocol using 2 different stimuli (Ea-b) or twice the same stimuli (Ea-a) with 3 different time intervals (dt) of 0.2 s, 0.5 s, and 1 s. **Significant difference at the $P < 0.005$ level (Mann-Whitney U-test; 10 Ea-a and 16 Ea-b stimulated facets and recording locations in $n = 4$ animals). Adapted from ref. [16].